DOI: 10.19884/j.1672-5220.202409007

Dynamic Analysis of Horizontal Servo System in Suspension Gravity Compensation System

WANG Wanqing[1], WANG Qingxia[1,3*], YANG Shuai[2], LI Na[2], HUANG Shunzhou[2,3]
1. College of Mechanical Engineering, Donghua University, Shanghai 201620, China
2. Shanghai Aerospace Equipments Manufacturer Co., Ltd., Shanghai 200245, China
3. Shanghai Aerospace Process and Equipment Engineering and Technology Research Center, Shanghai 200245, China

Abstract: A new suspension gravity compensation system has been developed to alleviate the gravity effects on a two-dimensional (2D) deployable mechanism for ground verification. Considering the rigid-flexible coupling of both the rotating servo and the suspension system, a multi-body dynamic model simulating their integration is established using Lagrange's equation. To mitigate instantaneous impact forces due to significant non-plumb effects from passive following in the horizontal direction, an elastic element is added in series with the rope in the vertical suspension system. The dynamic response of this elastic element relative to the rotating servo system is analyzed by the ADAMS software. Simulation results show that the compensating error decreases significantly from 45% to 0.31% when incorporating elastic elements compared to scenarios without such elements. Additionally, low-stiffness elastic elements demonstrate a higher compensating error than high-stiffness ones. A spring with a stiffness coefficient of 6 N/mm is selected in the experiment, ensuring that compensating error meets the design specification of 5%.

Keywords: suspension gravity compensation; passive servo system; flexible-rigid coupling model; series elastic element
CLC number: V216.8 **Document code**: A
Article ID: 1672-5220(2025)01-0029-12

Open Science Identity (OSID)

0 Introduction

The space deployable mechanism is a critical component of spacecraft, including antennas and spaceborne radars. Its successful deployment is essential for the normal operation of the spacecraft in the space environment. Consequently, conducting microgravity deployment experiments under ground conditions is imperative. In the suspension method, the system is connected via a rope suspension system, and the system's gravity is counteracted by the rope tension, thereby simulating a weightless environment[1]. Given that there is no time constraint on the gravity compensation system and three-dimensional (3D) spatial simulation can be achieved, the suspension method has been widely adopted in ground simulation experiments for deployable mechanisms[2-4].

Suspension methods can be divided into passive and active types, depending on whether the subsystem providing the gravity compensation force has active driving systems like motors and electric cylinders[5-6]. Passive low-gravity simulation typically uses rope suspension or counterweight suspension, with a simple structure, constant tension and high reliability. However, due to friction within the suspension system and the additional inertial forces during the object's vertical acceleration or deceleration, it is challenging to enhance the simulation accuracy of low-gravity environments[7-8]. In contrast, active suspension systems use actuators such as motors, electric cylinders and pneumatic springs to provide the rope tension. These systems implement servo closed-loop tension control to achieve active suspension without generating additional inertia during the movement of deployable mechanisms. This approach facilitates effective gravity balance within the required precision[9-11]. Nevertheless, deployable mechanisms often necessitate rigorous structural design for reliability and may even require redundancy in critical components[12-13]. Furthermore, in suspension simulation, either passive sliding systems or active position tracking systems are typically designed to follow the lifting point's position. This design enables accurate simulation of low-gravity environments in both two-dimensional (2D) and 3D spaces.

In recent years, domestic researchers have conducted various studies on ground simulation of low-gravity or weightless environments. Qiao et al.[14] developed a passive exoskeleton system for astronaut low-gravity walking simulation training, using a spring parallelogram system as its core unit. This system encompasses the human trunk and limbs, achieving a gravity-balancing exoskeleton training framework that simulates the low-gravity environment on Earth through simple passive control methods. However, the additional inertia

Received date: 2024-09-20
* Correspondence should be addressed to WANG Qingxia, email: wqxia@dhu.edu.cn
Citation: WANG W Q, WANG Q X, YANG S, et al. Dynamic analysis of horizontal servo system in suspension gravity compensation system[J]. *Journal of Donghua University (English Edition)*, 2025, 42(1): 29-40.

introduced by this design, along with the sway and tilt caused by suspension ropes, significantly affects the experimental results. Liu[15] developed a passive gravity compensation technology for mobile robots operating on the lunar surface, based on the principle of static equilibrium. This technology uses the elastic potential energy within springs to offset the gravity potential energy acting on the mobile robot, thereby achieving effective gravity compensation during various postural movements of the robot. Xiang[16] studied the active single sling suspension low-gravity training system. The system can track the trainer's movements in real time and maintain a consistent direction for the compensation tension. However, it suffers from significant inertia due to the linear guide, resulting in considerable impact disturbances.

This study introduces the design of a hybrid test system that integrates both active and passive systems. Specifically, it combines a passive servo system in the horizontal direction with an active suspension system in the vertical direction. The elastic potential energy stored within the spring is fully used. When acceleration occurs, an angle induced by the rope may compromise precision in gravity compensation. Such conditions could also lead to resonance between the spring and the system being compensated. The electric cylinder can adjust its compensation tension based on feedback from tension sensors, thereby mitigating additional inertia introduced by oscillations of the suspension rope. Furthermore, using a polar coordinate rotary structure allows for adaptation to impacts experienced during movement along guide rails. Additionally, incorporating a spring into the vertical suspension system helps to mitigate disturbances generated during motion. The suspension gravity compensation system features elastic elements oriented vertically and a long rope suspension positioned horizontally, characterizing it as a typical underactuated system[17-18]. Moreover, the nonlinear motion of the deployable mechanisms interacts with flexible components exhibiting significant slenderness ratios, such as the boom of the gravity compensation system. This interaction makes it challenging to both maintain a constant suspension tension and accurately track target positions. In fact, within a suspension gravity compensation system comprising suspension systems, the rigid-flexible coupling behavior between the movement of the rope and the motion of the deployable mechanisms is particularly significant in the test. Consequently, it is essential to conduct dynamic modeling and simulation of the system to optimize its design for improved performance characteristics in gravity compensation. In this study, we employ multi-body dynamics methods to establish a comprehensive dynamic model of the system followed by simulation calculations and experimental validation.

1 Dynamic Modeling

This study aims to develop a suspension gravity compensation system for ground studies of the analog antenna pointing mechanism (shown in Fig. 1(a)). This system comprises a horizontal rotation servo system, a horizontal linear servo system and a vertical servo system. The vertical servo system consists of an electric cylinder, an inclination sensor, a tension sensor and an elastic element, all connected in series via a rope. The upper end is connected to the pulley on the horizontal linear servo system while the lower end connects to the analog antenna pointing mechanism. This configuration enables suspension of the analog antenna pointing mechanism. The gravity effects on the analog antenna pointing mechanism are counteracted by the tension balance of the rope, thereby mitigating the effects of gravity. Simultaneously, this suspension gravity compensation system is integrated with the analog antenna pointing mechanism to track its position accurately. This ensures that the vertical servo system consistently points vertically towards the mass center of the suspended object.

The suspension gravity compensation system exhibits three types of motion: horizontal rotation, planar translation and pitch in the vertical plane. Among these, horizontal rotation and planar translation are classified as passive following motions, while the pitch in the vertical plane is considered as a mixed following motion that incorporates both horizontal passive and vertical active components. The precision of the tension balance in the suspension gravity compensation system depends mainly on the positional accuracy of the following system and the gravity compensation accuracy of the vertical servo system. In practice, the presence of friction and mechanical clearance within the system leads to asynchronous rotation. This phenomenon ultimately manifests in the rope, resulting in a swing angle that causes a deviation of the gravity compensation direction from the vertical direction. Therefore, it is essential to conduct dynamic modeling and simulation of the test system to analyze both its unloading capacity for gravity compensation and various factors influencing its dynamic characteristics.

Based on the multi-body dynamics method, a comprehensive dynamic model of the deployable mechanism and suspension gravity compensation system was established, as shown in Fig. 1(b). In scenarios involving high loads or rapid movements, friction at joints can significantly alter both motion states and energy losses within the system. Moreover, the material deformation under dynamic loading or substantial deformation may hinder accurate representation of the mechanical behavior within models, potentially leading to deviations in calculated results. Because the rotation speed of the deployable mechanism of the target object is 0.5 (°)/s and the mass is 30 kg, which are relatively low, the material properties of each component are assumed to be uniform, and for the time being, friction and clearance at the joints of the deployable mechanism are not taken into account. A coordinate system is established as shown in Fig. 2 for theoretical modeling and description. During simulation, x, y, l, θ_x and θ_y are defined as the degrees of freedom of the system. x represents a controllable active degree of freedom driven by a motor. l is

actively influenced by the output tension from an electric cylinder, which can be regarded as a controllable semi-active degree of freedom. Conversely, y, θ_x and θ_y constitute passive degrees of freedom that lack direct control via driving tensions. k is defined as the stiffness of the elastic element. F_r and F_{rz} denote the forces in the rope of the vertical servo system and its vertical component, respectively. P' and P are the upper and the lower lifting points, respectively. r_a is the rotation radius of P', and r_t is the rotation radius of P. $X_{P'}$ is the distance that the pulley moves along the guide rail in the rotation process. m is the mass of the analog antenna pointing mechanism. Thus, it can be concluded that this system qualifies as a multi-body underactuated system.

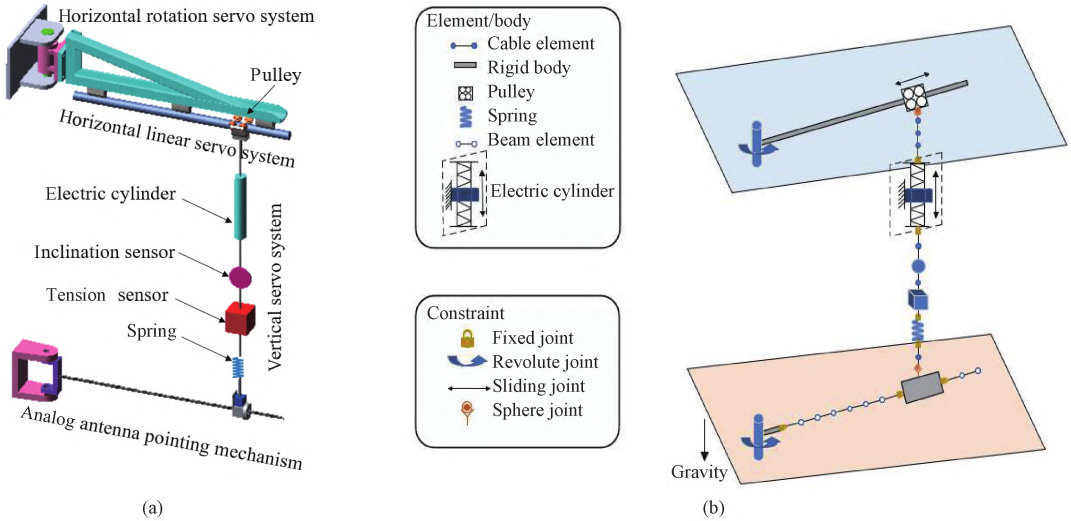

Fig. 1 Model of suspension gravity compensation system: (a) 3D design model; (b) physical model

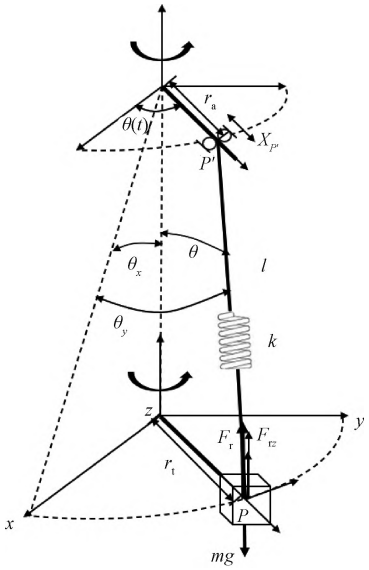

Fig. 2 Coordinate system of suspension gravity compensation system

In the multi-body dynamic model, the horizonal rotation servo system is simulated through the transmission dynamics of a screw-nut pair, with its front-end load being represented by the analog antenna pointing mechanism. In the horizontal rotation servo system, the guide rail and pulley are modeled using rigid body elements. Meanwhile, the fixed and sliding pairs are represented with specific constraints.

In the vertical servo system, the electric cylinder, tension sensor and spring are interconnected via a rope. The telescopic push rod of the electric cylinder facilitates movement of the rope. During simulation deployment, the suspension gravity compensation system not only generates rotation in the horizontal plane but also exhibits non-plumb effects. Additionally, under the influence of its own weight and unloading heavy objects, minor elastic vibrations occur along the direction of the rope.

According to Fig. 2, the coordinates of any point within the suspension gravity compensation system in the inertial coordinate system O-xyz is

$$\begin{cases} x_l = x_P - (l + \mu_f)\sin\theta_x, \\ y_l = y_P - (l + \mu_f)\cos\theta_x \sin\theta_y, \\ z_l = z_P + (l + \mu_f)\cos\theta_x \cos\theta_y, \end{cases} \tag{1}$$

where x_P, y_P and z_P are the spatial coordinates of the lower lifting point P of the suspension gravity compensation system in the inertial coordinate system O-xyz; x_l, y_l and z_l are the spatial coordinates of any point along the suspension gravity compensation system in the inertial coordinate system O-xyz. Since this point coincides with the center of the analog antenna pointing mechanism in the horizontal plane, the position vector under the rotating coordinate system can be denoted as $[x \quad y \quad z \quad l] = [0 \quad 0 \quad 0 \quad -l_0]$, where l_0 represents the length of the rope. μ_f is the elastic deformation at any point within a unit segment of the rope in the suspension gravity compensation system and can be expressed as

$$\mu_f = \boldsymbol{N}\boldsymbol{q}_e, \tag{2}$$

where $\boldsymbol{q}_e$ is the rope unit node displacement column vector; $\boldsymbol{N}$ denotes the element form function matrix.

The velocity of the point in the generalized coordinate system is

$$\begin{cases}\dot{x}_l = \dot{x} + \dot{l}\sin\theta_x + l\cos\theta_x\dot{\theta}_x + \boldsymbol{N}\boldsymbol{q}_e\cos\theta_x\dot{\theta}_x + \boldsymbol{N}\dot{\boldsymbol{q}}_e\sin\theta_x,\\ \dot{y}_l = \dot{y} + (\dot{l} + \boldsymbol{N}\dot{\boldsymbol{q}}_e)\cos\theta_x\sin\theta_y - (l + \boldsymbol{N}\boldsymbol{q}_e)(\sin\theta_x\sin\theta_y\dot{\theta}_x + \cos\theta_x\cos\theta_y\dot{\theta}_y),\\ \dot{z}_l = (\dot{l} + \boldsymbol{N}\dot{\boldsymbol{q}}_e)\cos\theta_x\cos\theta_y - (l + \boldsymbol{N}\boldsymbol{q}_e)\sin\theta_x\cos\theta_y\dot{\theta}_x - (l + \boldsymbol{N}\boldsymbol{q}_e)\cos\theta_x\sin\theta_y\dot{\theta}_y.\end{cases} \tag{3}$$

To enhance the clarity of the model derivation, Eq. (1) is now reformulated in the vector form:

$$\boldsymbol{r}_l = \boldsymbol{r}_t + \boldsymbol{R}_l(l + \boldsymbol{N}\boldsymbol{q}_e), \tag{4}$$

where $\boldsymbol{r}_t$ is the vector diameter of the lower lifting point P of the suspension gravity compensation system in the inertial coordinate system at the current time; $\boldsymbol{r}_l$ is the vector diameter of any point on the suspension gravity compensation system; $\boldsymbol{R}_l$ is the transformation matrix between the dynamic coordinate system and the revolving coordinate system of the suspension gravity compensation system.

$$\boldsymbol{R}_l = \begin{bmatrix}\cos\beta & \sin\beta\sin\alpha & 0\\ 0 & 0 & 0\\ 0 & 0 & 0\end{bmatrix}, \tag{5}$$

where α and β are the Euler angles of the rope rotating around the X axis and Y axis in the dynamic coordinate system, respectively.

Thus, the velocity of any point on the suspension gravity compensation system in the inertial coordinate system is

$$\dot{\boldsymbol{r}}_l = \dot{\boldsymbol{r}}_t + \boldsymbol{R}_l\boldsymbol{\Omega}_l(l + \boldsymbol{N}\boldsymbol{q}_e) + \boldsymbol{R}_l\boldsymbol{N}\dot{\boldsymbol{q}}_e, \tag{6}$$

where $\boldsymbol{\Omega}_l$ is the antisymmetric matrix:

$$\boldsymbol{\Omega}_l = \begin{bmatrix}0 & \sin\alpha & 0\\ 0 & 0 & 0\\ 0 & 0 & 0\end{bmatrix}. \tag{7}$$

According to Eq. (6), the velocity of any point on the suspension gravity compensation system encompasses both the macro-level rotation and swinging of the rope, as well as the micro-level elastic vibrations of the rope. Consequently, the unit kinetic energy of the suspension gravity compensation system T_l is

$$\begin{aligned}T_l = \frac{1}{2}m_l\dot{\boldsymbol{r}}_l^{\mathrm{T}}\dot{\boldsymbol{r}}_l = \frac{1}{2}\rho\int_V\dot{\boldsymbol{r}}_l\dot{\boldsymbol{r}}_l\mathrm{d}V = \frac{1}{2}\rho\int_V[\dot{\boldsymbol{r}}_t + \boldsymbol{R}_l\boldsymbol{\Omega}_l(l + \boldsymbol{N}\boldsymbol{q}_e) + \boldsymbol{R}_l\boldsymbol{N}\dot{\boldsymbol{q}}_e]^{\mathrm{T}}\cdot\\ [\dot{\boldsymbol{r}}_t + \boldsymbol{R}_l\boldsymbol{\Omega}_l(l + \boldsymbol{N}\boldsymbol{q}_e) + \boldsymbol{R}_l\boldsymbol{N}\dot{\boldsymbol{q}}_e]\mathrm{d}V = \boldsymbol{T}_l^{\mathrm{r}} + \boldsymbol{T}_l^{\mathrm{s}} + \boldsymbol{T}_l^{\mathrm{r,s}} + \boldsymbol{T}_l^{\mathrm{e}} + \boldsymbol{T}_l^{\mathrm{r,e}} + \boldsymbol{T}_l^{\mathrm{s,e}},\end{aligned} \tag{8}$$

where ρ is the density of the rope; the superscripts r, s and e denote rotation, oscillation and elastic vibration, respectively. The amplitude of the elastic vibration is relatively small, and thus its impact on rotation and oscillation can be disregarded, namely $\boldsymbol{T}_l^{\mathrm{r,e}} = \boldsymbol{T}_l^{\mathrm{s,e}} = 0$.

According to Eqs. (6) and (8), the kinetic energy generated by rotation and oscillation of the suspension gravity compensation system $T_{l,\mathrm{I}}$ can be further obtained:

$$\begin{aligned}\boldsymbol{T}_{l,\mathrm{I}} = \frac{1}{2}m_l(\dot{\boldsymbol{r}}_t + \dot{\boldsymbol{R}}_l\boldsymbol{\Omega}_l l)^{\mathrm{T}}(\dot{\boldsymbol{r}}_t + \dot{\boldsymbol{R}}_l\boldsymbol{\Omega}_l l) =\\ \frac{1}{2}\begin{bmatrix}\dot{\boldsymbol{r}}_t\\ \dot{\boldsymbol{\theta}}_{\alpha\beta}\end{bmatrix}\begin{bmatrix}\boldsymbol{M}_{rr} & \boldsymbol{M}_{r\theta}\\ \boldsymbol{M}_{\theta r} & \boldsymbol{M}_{\theta\theta}\end{bmatrix}\begin{bmatrix}\dot{\boldsymbol{r}}_t\\ \dot{\boldsymbol{\theta}}_{\alpha\beta}\end{bmatrix},\end{aligned} \tag{9}$$

where m_l is the mass of the vertical servo system; $\boldsymbol{\theta}_{\alpha\beta}$ is the column vector of the Euler angle and $\boldsymbol{\theta}_{\alpha\beta} = [\alpha \quad \beta]^{\mathrm{T}}$; $\boldsymbol{M}_{rr}$ and $\boldsymbol{M}_{\theta\theta}$ represent the mass matrices associated with the rigid body rotation and swinging of the suspension gravity compensation system, respectively; $\boldsymbol{M}_{r\theta}$ and $\boldsymbol{M}_{\theta r}$ are the coupled quality matrices of the rigid body rotation and swinging of the suspension gravity compensation system, respectively, and $\boldsymbol{M}_{r\theta} = \boldsymbol{M}_{\theta r}^{\mathrm{T}}$.

Additionally, from Eqs. (6) and (8), the kinetic energy of the rope when elastic vibration occurs $T_{l,\mathrm{II}}$ can be obtained:

$$T_{l,\mathrm{II}} = \frac{1}{2}\rho\int_V[\boldsymbol{\Omega}_l\boldsymbol{N}\boldsymbol{q}_e + \boldsymbol{N}\dot{\boldsymbol{q}}_e]^{\mathrm{T}}\cdot[\boldsymbol{\Omega}_l\boldsymbol{N}\boldsymbol{q}_e + \boldsymbol{N}\dot{\boldsymbol{q}}_e]\,\mathrm{d}V. \tag{10}$$

Considering the rope in the suspension unit as a linear flexible body element, according to the Timoshenko beam theory, its elastic potential energy[1] U_e is

$$U_e = \int_V(\boldsymbol{\sigma} + \boldsymbol{\sigma}_0):\delta(\boldsymbol{\varepsilon}_l)\mathrm{d}V = \frac{1}{2}(\boldsymbol{w}^e)^{\mathrm{T}}(\boldsymbol{K}_L^e + \boldsymbol{K}_L^g)\boldsymbol{q}_e, \tag{11}$$

where σ is the strain tensor induced by the linear strain; σ_0 is the initial strain tensor induced by the self-weight and unloading weight of the suspension gravity compensation system; $\boldsymbol{\varepsilon}_l$ is the linear strain tensor of the rope; $\boldsymbol{w}^e$ is the displacement vector of the rope unit node; $\boldsymbol{K}_L^e$ and $\boldsymbol{K}_L^g$ are the element elastic stiffness matrix and geometric stiffness matrix, respectively.

Set the plane simulating the rotation of the target object as the reference point for the potential energy. Considering the mass of the rope m_r, the conservative tension of the cable tension f_l is incorporated into the system's potential energy U_h:

$$U_h = m_r g(z_l - l\cos\theta_x\cos\theta_y) + f_l l. \tag{12}$$

The rotating guide rail is treated as a rigid body in this study, meaning that its deflection effects are not taken into account. Suppose that the vector diameter of any point on the rotating guide rail in the inertial coordinate system is $\boldsymbol{r}_\alpha$, and the angle of the rotating guide rail in the horizontal rotation servo system is $\theta(t)$. The angular velocity of this point is $\omega = \dot{\theta}(t)$. Thus, the

kinetic energy of the rotating guide rail can be described as

$$T_{l,\mathrm{II}} = \frac{1}{2}\rho' \int_V [\boldsymbol{\Omega}_l \boldsymbol{N}\boldsymbol{q}_e + \boldsymbol{N}\dot{\boldsymbol{q}}_e]^{\mathrm{T}} \cdot [\boldsymbol{\Omega}_l \boldsymbol{N}\boldsymbol{q}_e + \boldsymbol{N}\dot{\boldsymbol{q}}_e] \mathrm{d}V, \quad (13)$$

where ρ' is the density of the rotating arm.

Considering the damping terms $D_{\theta x}$, D_β and D_l arising from friction during the sliding of the pulley on the guide rail, as well as from the damping caused by the elastic vibration of the rope, the dynamic equations describing the multi-body motion process of the system can be written by using the first Lagrange equation[1]:

$$\begin{cases} \dfrac{\mathrm{d}}{\mathrm{d}t}\left(\dfrac{\partial L}{\partial \dot{x}}\right) - \dfrac{\partial L}{\partial x} = f_x, \\ \dfrac{\mathrm{d}}{\mathrm{d}t}\left(\dfrac{\partial L}{\partial \dot{y}}\right) - \dfrac{\partial L}{\partial y} = f_y, \\ \dfrac{\mathrm{d}}{\mathrm{d}t}\left(\dfrac{\partial L}{\partial \dot{l}}\right) - \dfrac{\partial L}{\partial l} = f_z - D_l \dot{l}, \\ \dfrac{\mathrm{d}}{\mathrm{d}t}\left(\dfrac{\partial L}{\partial \dot{\theta}_x}\right) - \dfrac{\partial L}{\partial \theta_x} = -D_{\theta x}\dot{\theta}_x, \\ \dfrac{\mathrm{d}}{\mathrm{d}t}\left(\dfrac{\partial L}{\partial \dot{\theta}_y}\right) - \dfrac{\partial L}{\partial \theta_y} = -D_{\theta y}\dot{\theta}_y, \end{cases} \quad (14)$$

where L is the Lagrange operator, $L = T - U$, and T and U are the kinetic and potential energies of the suspension gravity compensation system, respectively; f_x and f_y represent the driving tensions of the output of the deployable mechanism on generalized degrees of freedom x and y, respectively.

If the generalized state of the suspension gravity compensation system is denoted by $\boldsymbol{q} = [x \quad y \quad l \quad \theta_x \quad \theta_y]^{\mathrm{T}}$, then considering the kinetic energy, potential energy and dynamic equation of the system comprehensively, rewrite Eq. (13):

$$\boldsymbol{M}(\boldsymbol{q})\ddot{\boldsymbol{q}} + \boldsymbol{D}\dot{\boldsymbol{q}} + C(\boldsymbol{q},\dot{\boldsymbol{q}})\dot{\boldsymbol{q}} + g(\boldsymbol{q}) = \boldsymbol{\tau}, \quad (15)$$

where $\boldsymbol{M}(\boldsymbol{q})\ddot{\boldsymbol{q}} = \begin{bmatrix} \boldsymbol{M}_{11}(\boldsymbol{q}) & \boldsymbol{M}_{12}(\boldsymbol{q}) \\ \boldsymbol{M}_{21}(\boldsymbol{q}) & \boldsymbol{M}_{22}(\boldsymbol{q}) \end{bmatrix}$ and $\boldsymbol{D} = [0 \quad 0 \quad D_l \quad D_{\theta x} \quad D_{\theta y}]$ represent the inertia and damping of the system, respectively; $C(\boldsymbol{q}) = \begin{bmatrix} C_{11}(\boldsymbol{q}) & C_{12}(\boldsymbol{q}) \\ C_{21}(\boldsymbol{q}) & C_{22}(\boldsymbol{q}) \end{bmatrix}$ represents the Coriolis tension and centrifugal tension matrix generated by the coupling of the system deformation and rotation motion; $g(\boldsymbol{q})$ is the total stiffness matrix considering elastic elements and rotary centrifugal tensions of the system; $\boldsymbol{\tau} = [f_x \quad f_y \quad f_z \quad 0 \quad 0]^{\mathrm{T}}$ denotes the controlling tension and external tension matrix.

2 Dynamic Simulation Analysis

Based on the aforementioned multi-body dynamics model, this study investigates the performance of the deployable mechanism for the suspension gravity compensation system. Initially, the ADAMS dynamic simulation software is used to simulate the system. The structure parameters of the simulator-gravity compensation system are presented in Table 1. Notably, the mass of the simulated deployable mechanism is approximately 30 kg, and the target value for gravity compensation is 300 N.

Table 1 Structure parameters of simulator-gravity compensation system

Parameter	Value
Simulated deployable radius/mm	750
Maximum overhang length of guide rail/mm	1 000
Span between two bearings on the rotating shaft/mm	350
Maximum dimensions of electric cylinder and sensor/mm	350
Rotating pair dynamic factor	0.008
Static friction factor	0.012
Dynamic friction factor between the pulley and the guide rail	0.008
Static friction factor between the pulley and the guide rail	0.012
Distance between two points of vertical servo system/mm	1 800

The rigid-flexible coupling model of the suspension gravity compensation system was established in ADAMS, with the flow chart illustrated in Fig. 3. Initially, the suspension gravity compensation system was modeled using 3D modeling software. Subsequently, components requiring flexibility were analyzed and modified using ANSYS. The rigid and flexible units were then integrated into ADAMS, where dynamic simulations of the virtual prototype of the system were conducted after incorporating constraint pairs and drives within the ADAMS environment.

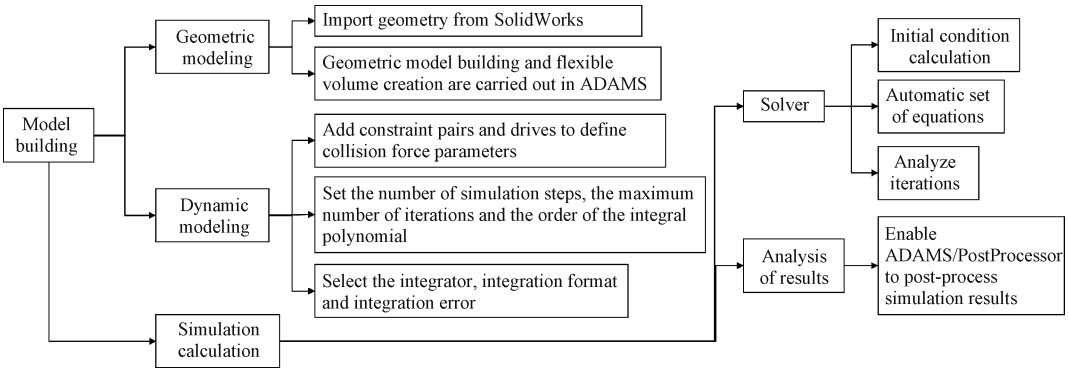

Fig. 3 Simulation flow chart of ADAMS

When the simulator-gravity compensation system compensates for the gravity of the simulated deployable mechanisms, the rope can be considered equivalent to a spring with a high elastic coefficient. When the target object begins to deploy or when the suspension tension system tilts, an instantaneous acceleration in the direction of the plumb weight is induced throughout the entire compensation system. This results in an immediate impact tension within the system, which not only diminishes its stability but also generates additional torque[1] on the target object. Consequently, the structural design incorporates elastic elements and series configurations of the rope.

To thoroughly investigate the role of series elastic elements, active control via electric cylinders is not implemented in the simulation model. Instead, they are treated as rigid bodies. In this study, we concentrate on examining how series elastic elements dynamically influence both the swing angle and gravity compensation associated with the rope.

For the sake of clarity, the following symbols used in this text are described uniformly. Let F_d represent the anticipated gravity compensation tension.

The gravity compensating error is represented by a parameter η:

$$\eta = \frac{|F_{rz} - F_d|}{F_d}. \tag{16}$$

2.1 Influence of inelastic elements

Figure 4 illustrates the variations in the vertical component of tensions and inclination angles of the rope during the passive following process of the horizontal rotation servo system, both with and without series elastic elements. During the initial phase of deployment, both the inclination angle and tension of the rope gradually increase. This observation indicates that while the simulated deployable mechanism rotates, the system fails to keep pace effectively, leading to a gradual lagging of the upper lifting point P' behind the lower lifting point P. After a certain period, as the simulated deployable mechanism continues its unfolding process, there is no further increase in the rope inclination. Instead, it stabilizes around a specific value. The vertical component of the rope tension exhibits a similar trend. For clarity in description, these stages can be categorized into an initial following stage and a continuous following stage.

Specifically, during the initial following stage, when no series elastic element is employed, the maximum hysteresis angle at the upper lifting point P' of the suspension gravity compensation system is approximately 0.80° in comparison to that at the lower lifting point P. The maximum vertical component of the rope tension can reach around 455 N. At about 4.5 s, the system transitions into a continuous following stage, and the tangential component of the rope angle exhibits a decreasing trend with an amplitude ranging between 0.60° and 0.70°. Concurrently, the vertical component of the rope tension oscillates around 435 N. Upon introducing the elastic element with a stiffness coefficient of 6 N/mm, the hysteresis angle at the upper lifting point P' relative to the lower lifting point P decreases to a maximum of approximately 0.70° during the initial following stage. Simultaneously, the vertical component of the rope tension diminishes to a peak value of 301 N. After about 4.0 s, it also enters into a continuous following stage, and there is a continued decrease in tangential components of the rope angle with an amplitude ranging from 0.45° to 0.60°. At this juncture, fluctuations in vertical components of the rope tension stabilize around 301 N. The series elastic elements could decrease the compensating error of the device from 45% to 0.31%.

Figure 4(b) illustrates that series elastic elements have no effect on the displacement of the pulley on the guide rail. Figures 4(c) and 4(d) illustrate the effects of the horizontal rotation servo system in the normal direction. It is evident that the normal component of the rope angle, with 0 as the reference value, exhibits a sinusoidal wave pattern. This behavior indicates that there is a slight displacement of the block within the horizontal rotation servo system along the guide rail. Notably, this phenomenon appears to be largely independent of whether an elastic element is connected in the suspension gravity compensation system.

Furthermore, it can be observed that when the vertical servo system does not incorporate a series elastic element, the vertical component of the rope within the horizontal rotation servo system significantly exceeds the

anticipated compensation tension during passive following operations. Consequently, this results in a gravity compensating error that far surpasses the 5% threshold established by ground test requirements.

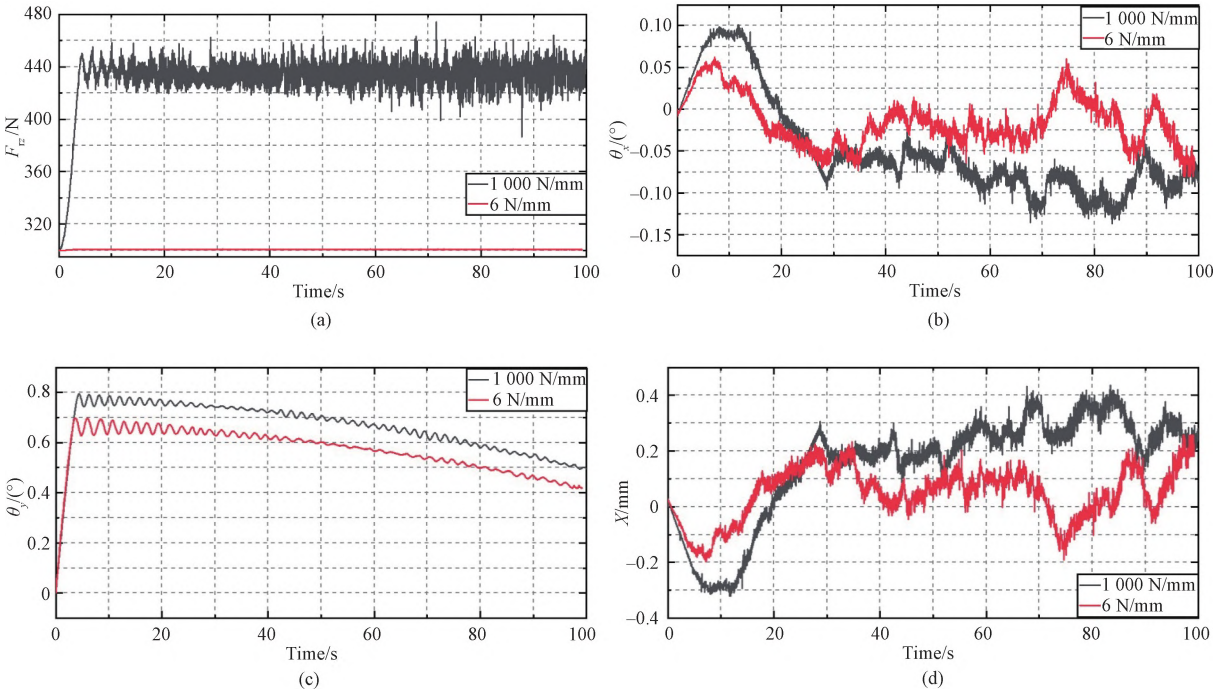

Fig. 4 Response curves of suspension gravity compensation system with (k=1 000 N/mm) or without (k=6 N/mm) an elastic element: (a) vertical component of tension; (b) normal inclination angle; (c) tangential inclination angle; (d) displacement of pulley

According to the multi-body dynamic model established above, the accuracy of the horizontal rotation servo system is significantly influenced by the system parameters listed in Table 1, particularly the system's stiffness, damping and friction. Among these factors, the system's stiffness and the damping are closely related to the mechanical structure and materials used, and approximate values can be derived through theoretical calculations and experiments. However, it is important to note that the sliding friction between rotating pairs primarily arises from the disparity between static friction and dynamic friction as well as from the Stribeck effect observed in low-speed regions[1]. This phenomenon impacts dynamic following performance. During the initial phase of the simulated deployable motion, static friction occurs between the rotating shaft and its seat. Consequently, the upper lifting point gradually lags behind the lower lifting point over a brief period. This results in a rapid increase in the relative angular displacement. Once the circumferential component tension generated by tilting of the rope within the suspension gravity compensation system enables overcoming static frictional tensions, causing relative rotation, the moving part will begin to accelerate. If the elastic tension surpasses the damping tension, this acceleration will be positive; conversely, it will be negative.

At the same time, the system can be represented as a single degree of freedom mechanical vibration system comprising two springs and viscous damping elements connected in series. Let the stiffness coefficients of the two springs be k_1 and k_2, respectively. The total stiffness of the system k_t satisfies

$$\frac{1}{k_t}=\frac{1}{k_1}+\frac{1}{k_2}. \tag{17}$$

From Eq. (17), it can be observed that when the system does not incorporate elastic components, the total stiffness of the system is approximately equivalent to the stiffness of the rope. When a rope is integrated with a spring, the overall stiffness coefficient of the system closely resembles that of the spring.

If v_p denotes the vertical instantaneous speed of the suspension gravity compensation system and t denotes the electromechanical time constant of the electric cylinder, the interference tension F_d within this system is kv_pt. It is evident that an increase in the stiffness coefficient of the system results in a corresponding increase in the interference force.

If an impact load occurs within the system, the suspension tension will experience abrupt changes and the motor is unable to respond instantaneously. During this period, the disturbance in the suspension tension relies entirely on passive elastic elements for mitigation. Consequently, when these elastic elements are connected in series within the horizontal rotation servo system, a superior response effect is demonstrated as illustrated in Fig. 4.

It can be observed that the series elastic elements in

the vertical servo system effectively function as a low-pass filter. Through the above analysis, it is evident that tension impacts can be significantly suppressed, thereby reducing compensating errors associated with the suspension tension.

2.2 Influence of elastic elements with different stiffnesses on system

It needs further discussion to appropriately choose the spring stiffness for good rapid response ability. Therefore, the influence of elastic elements with different stiffnesses on the dynamic performance of the suspension gravity compensation system is simulated.

The stiffness of the spring is taken as $k=6$, 13, 20, 27 and 34 N/mm. Figure 5 shows the response curves under different stiffnesses of elastic elements. For the rope tension and its vertical component, the lower the stiffness of the elastic element, the longer the dynamic response time in the transient stage, but the smaller the maximum overshoot.

According to Fig. 6, the highest gravity compensating errors obtained in this example are 0.31%, 0.64%, 0.88%, 1.20% and 1.77%, respectively. This shows that the gravity compensating error is directly affected by the stiffness of the elastic element. The lower the stiffness, the lower the suspension tension compensating error. It shows that the elastic element with a lower stiffness can result in the lower oscillation amplitude, and the effect of gravity compensation is better.

According to Fig. 5(b), during the initial following stage in different stiffnesses of the spring, the upper lifting point on the horizontal rotation servo system gradually lags behind the lower lifting point in the direction of the circular rotation. This lag reaches its maximum value in about 7 s, measuring about 0.69°, 0.73°, 0.69°, 0.78° and 0.82°, respectively. Subsequently, the hysteresis angle decreases and oscillates around 0.65°, 0.58°, 0.55°, 0.57° and 0.68°, respectively. The following angle in the normal direction and the displacement curve of the pulley are observed to exhibit periodic oscillations, with a maximum fluctuation range of ±0.07° and a displacement variation of ±0.25 mm.

As illustrated in Figs. 5(c) and 5(d), the suspension gravity compensation system designed in this study consistently demonstrates hysteresis in the circumferential direction while exhibiting periodic fluctuation in the radial direction. Furthermore, the rotation following accuracy is not significantly influenced by the stiffness of the elastic element.

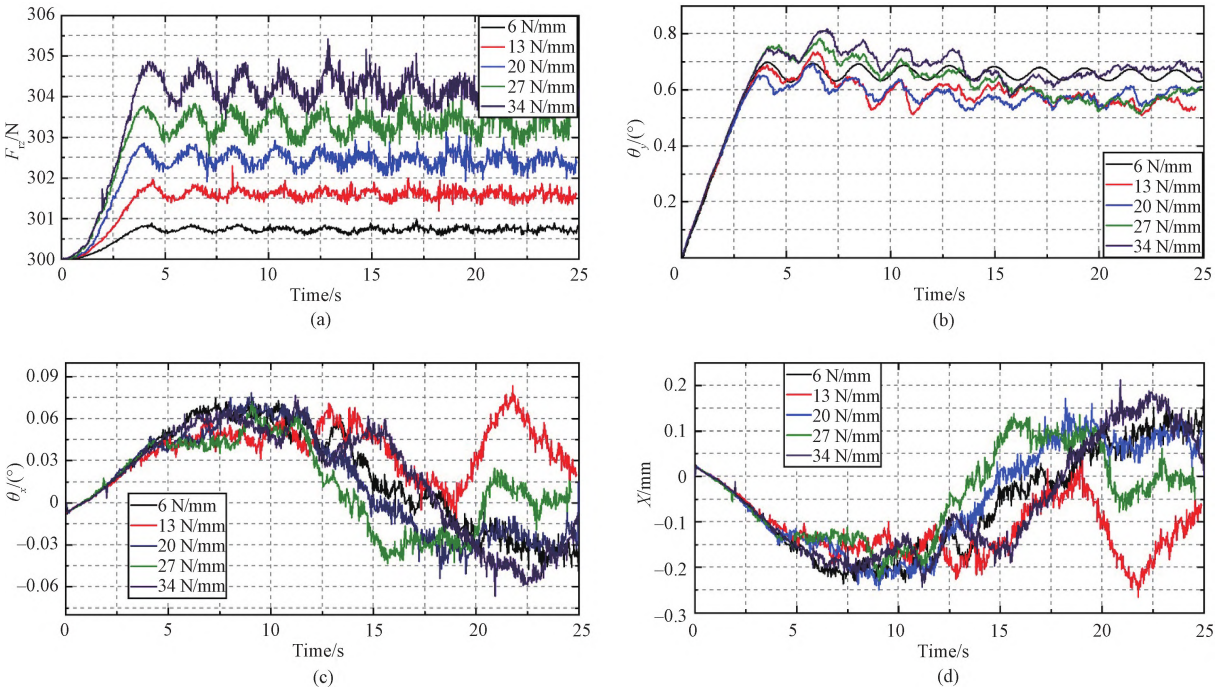

Fig. 5 Response curves of suspension gravity compensation system at different elastic element stiffnesses ($\omega = 0.5$ (°)/s): (a) vertical component of tension; (b) tangential inclination angle; (c) normal inclination angle; (d) displacement of pulley

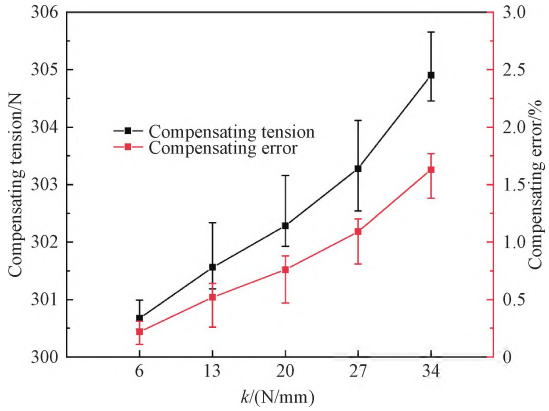

Fig. 6 Influence of different elastic element stiffnesses on response characteristics (ω =0.5 (°)/s)

Figure 7 shows the time response of the suspension gravity compensation system operating at a stiffness of 6 N/mm with the vertical servo system at different deployment speeds. As observed in Figs. 7 (a) and 7(b), an increase in the deployment speed leads to a significant rise in the maximum overshoot, despite a reduction in the rise time for both the rope tension and inclination responses. While the mean value of the vertical component of the rope tension remains relatively constant, there is a notable increase in the amplitude fluctuation range as the unwrapping speed escalates during continuous unwrapping operations. Concurrently, oscillation amplitudes for both normal inclination components and block displacements also exhibit an upward trend with the increasing deployment speed. This indicates that during the ground test, the horizontal linear servo system designed herein demonstrates enhanced passive following capabilities when simulating deployment mechanisms at lower speeds.

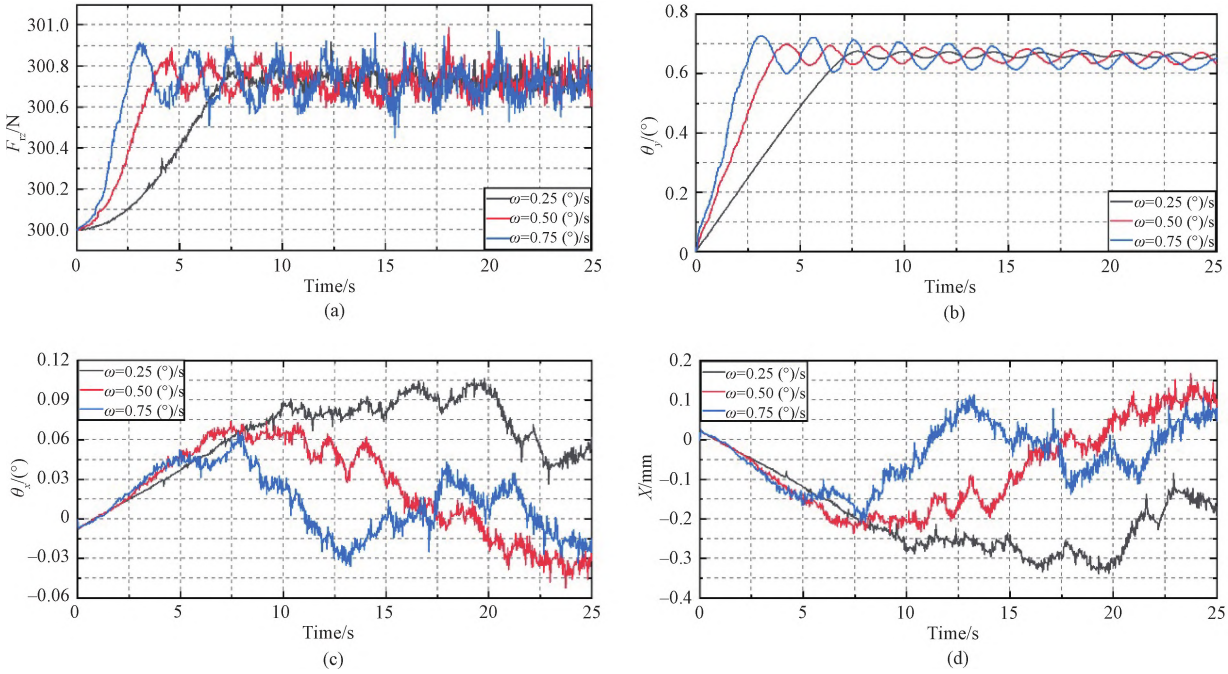

Fig. 7 Response curves of suspension gravity compensation system at different deployment speeds (k=6 N/mm): (a) vertical component of tension; (b) tangential inclination angle; (c) normal inclination angle; (d) displacement of pulley

2.3 Experimental test

The construction prototype of the suspension gravity compensation system for the ground test of the deployable mechansim is depicted in Fig. 8. The length of the rotating shaft is 350 mm, while the system is mounted on a guide rail via the pulley. It rotates horizontally around a rotating shaft through a guide rail, creating a rotation radius at the suspended point of 750 mm. Additionally, there is a vertical distance of 1 800 mm between both lifting points of the system, which aligns with that specified in the simulation model. Due to structural size limitations inherent to the simulated deployable platform, only horizontal rotating within a limited deployable range was simulated. In line with the rotational motion of the analog antenna pointing mechanism, an engineered rotary follower tracks its mass center trajectory while maintaining a coaxial rotation axis with its simulant. It allows for slight displacement caused by the pulley on the guide rail. The vertical servo system connects sequentially to an electric cylinder, a spring, a tension sensor and an inclination sensor via the rope. The electric cylinder applies the unloading tension to the simulated deployable mechanism, the tension sensor can monitor and record the rope tension in real time, and the inclination sensor records the rope inclination in the following process in real time.

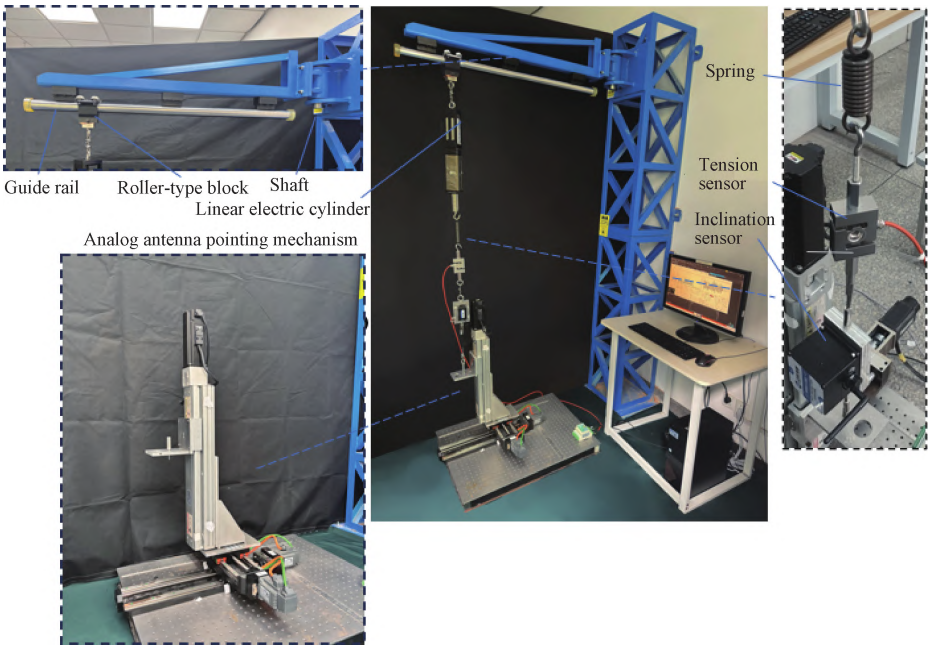

Fig. 8 Physical model of suspension gravity compensation system

According to the simulation results presented above, the suspension length is 1 800 mm and the stiffness of the elastic element is 6 N/mm. The analog antenna pointing mechanism initially swings forward by approximately 13° before returning back by an equal angle. The angular velocity recorded during this process is 0.5 (°)/s. Real-time output signals from both the tension sensor and the inclination sensor are obtained during experimentation, as illustrated in Fig. 9.

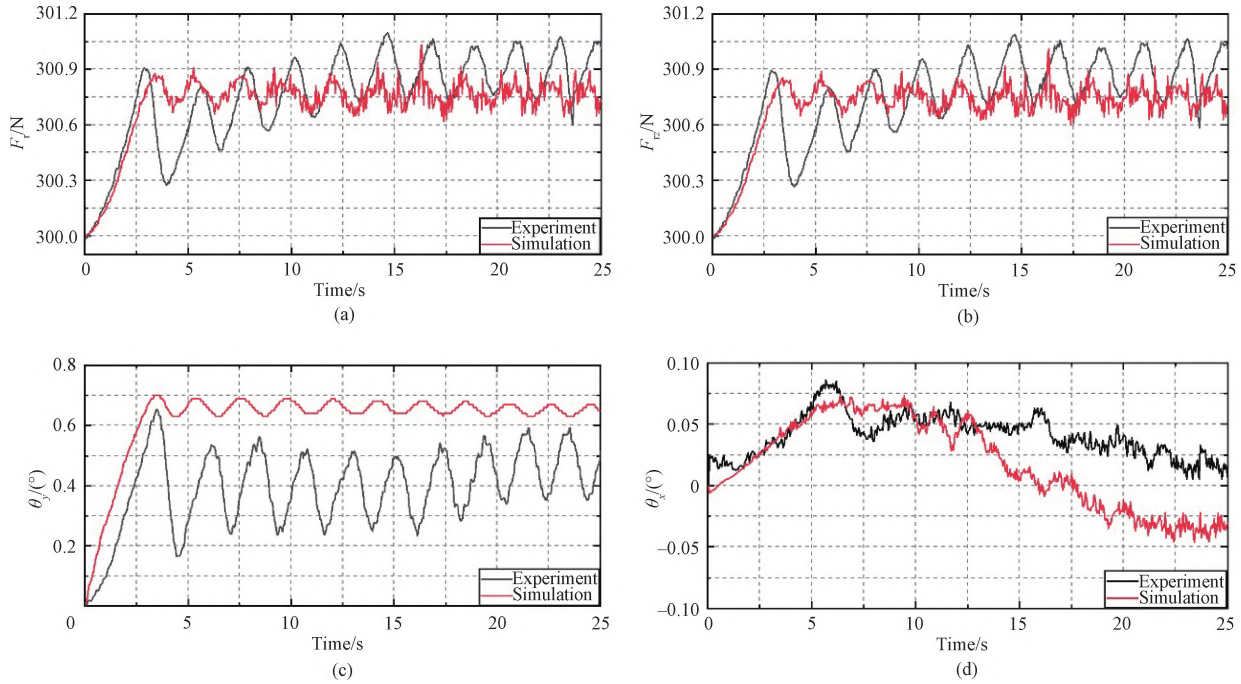

Fig. 9 Test results of suspension gravity compensation experiment: (a) tension in rope; (b) vertical component of tension; (c) tangential inclination angle; (d) normal inclination angle

The fluctuation amplitude of both the tension of the rope and the vertical component tension derived from simulated gravity compensation exceeds that calculated using the ADAMS model. However, their mean change trends are largely consistent. Notably, the angle of the rope measured experimentally is lower than that predicted by the ADAMS model. Upon further analysis, this discrepancy may be attributed to leveling compensating

errors encountered after installing the suspension gravity compensation system. Given that the experimental apparatus is relatively large in size, its installation and adjustment processes are inherently complex. The pulley generally adheres to a leveling design requirement of within 0.5 mm over a one-meter stroke distance. Furthermore, considering that the actual boundary conditions and load conditions might differ from the assumptions of the model, which leads to the inaccuracy of the dynamic response, the necessary nonlinear characteristics could be added to the study to enhance the accuracy of the model. Since the vibration of the equipment in the experimental environment can impact the reading of the sensor, the data can be acquired by using a shock absorbing table or through multiple experiments, and statistical analyses can be conducted to reduce accidental errors and enhance the reliability of the results. Although the error seems minor, it indicates that while providing a movement speed, the deployable mechanism also applies a slight horizontal tension. When this direction aligns with any horizontal inclination, it leads to a reduction in the actual rope inclination angle, and conversely there is an increase in the actual rope inclination angle.

3 Conclusions

The study focuses on the structural and motion characteristics of a ground-suspended simulation system for deployable mechanisms. A multi-body dynamics model has been established that comprehensively considers the rigid-flexible coupling features of both the horizontal linear servo system and the vertical servo system, as well as the effects of elastic deformation in the ropes. Dynamic simulation experiments demonstrate that the elastic elements effectively mitigate disturbances in the suspension gravity compensation system. By selecting appropriate spring stiffnesses, it is possible not only to reduce compensating errors but also to significantly enhance the following performance. The results from simulations and experiments indicate that the suspension gravity compensation system proposed in this study achieves a rotation following accuracy better than 1° under working conditions with a guide rail span of 1 m and a load mass of 30 kg. Additionally, its gravity unloading accuracy is approximately 97%, thereby meeting the requirement for at least 95% gravity unloading. This work provides an effective and reliable theoretical foundation for parameter optimization and control design within the system. In the future, an air bearing support may be used to design the gravity compensation system to achieve a higher unloading accuracy and a faster following effect, and more comprehensive dynamic behaviors are taken into account, such as nonlinear effects and time-varying characteristics. Also, the ANSYS Workbench and ADAMS co-simulation can be introduced to conduct more detailed modeling to reflect the actual working conditions.

References

[1] ZHOU M, ZHAN G H, SONG X D. Dynamic study on magnetic suspension microgravity simulation system [J]. *Journal of Dynamics and Control*, 2021, 19(6): 33-40. (in Chinese)

[2] LIU R Q, SHI C, GUO H, et al. Research and prospect of space deployable antenna mechanism [J]. *Journal of Mechanical Engineering*, 2020, 56(5): 1-12. (in Chinese)

[3] LIU C, TIAN Q, HU H Y. Efficient calculational method for dynamics of flexible multibody systems based on absolute nodal coordinates [J]. *Chinese Journal of Theoretical and Applied Mechanics*, 2010, 42(6): 1197-1205. (in Chinese)

[4] PENG Y, YANG J G, XIAO Y, et al. Gravity effect on deployment dynamics of astromesh[J]. *Engineering Mechanics*, 2018, 35(4): 226-234, 256.

[5] QUISENBERRY J, ARENA A. Discrete cable modeling and dynamic analysis [C]//The 44th AIAA Aerospace Sciences Meeting and Exhibit. Reno, Nevada: AIAA, 2006: 424.

[6] RYBUS T, SEWERYN K. Application of a planar air-bearing microgravity simulator for demonstration of operations required for an orbital capture with a manipulator [J]. *Acta Astronautica*, 2019, 155: 211-229.

[7] YUAN J P, ZHU Z X, MING Z F, et al. An innovative method for simulating microgravity effects through combining electromagnetic force and buoyancy[J]. *Advance in Space Research*, 2015, 56(2): 355-364.

[8] ZHU Z X, YUAN J P, SONG J Z, et al. An improved method for micro-G simulation with magnetism-buoyancy hybrid system[J]. *Advance in Space Research*, 2016, 57(12): 2548-2558.

[9] SUN C, CHEN S Y, YUAN J P, et al. A six-DOF buoyancy tank microgravity test bed with active drag compensation [J]. *Microgravity Science and Technology*, 2017, 29: 391-402.

[10] FISCHER A, PELLEGRIINO S. Interaction between gravity compensation suspension system and deployable structure[C]//The 39th AIAA/ASME/ASCE/AHS/ASC Structures, Structural Dynamics, and Materials Conference and Exhibit. Long Beach, USA: AIAA, 1998: 1835.

[11] KU N, HA S. Dynamic response analysis of heavy load lifting operation in shipyard using multi-cranes[J]. *Ocean Engineering*, 2014, 83: 63-75.

[12] CHAPPELL S P, NORCROSS J R, CLOWERS K G, et al. Final report of the integrated

parabolic flight test: effects of varying gravity, center of gravity, and mass on the movement biomechanics and operator compensation of ambulation and exploration tasks [R]. NASA/TP-2010-21637, 2010.
[13] NIKSIRAT P, DACA A, SKONIECZNY K. The effects of reduced-gravity on planetary rover mobility [J]. *The International Journal of Robotics Research*, 2020, 39(7): 797-811.
[14] QIAO B, CHEN Z P. Simulation of passive exoskeleton robot for astronaut low-gravity walking training [J]. *Journal of Astronautics*, 2014, 35(4): 474-480. (in Chinese)
[15] LIU W X. Research on passive gravity compensation technology of lunar mobile robot [D]. Beijing: Beijing University of Posts and Telecommunications, 2015. (in Chinese)
[16] XIANG S. Dynamic modeling and control analysis of suspended astronaut low gravity simulation system[D]. Harbin: Harbin Institute of Technology, 2015. (in Chinese)
[17] LIU J P, CHENG Z B, REN G X. An arbitrary Lagrangian-Eulerian formulation of a geometrically exact Timoshenko beam running through a tube [J]. *Acta Mechanica*, 2018, 229: 3161-3188.
[18] SHI J B, LIU Z Y, HONG J Z. Multi-body dynamics analysis of deployment of solar arrays with large deformation [J]. *Journal of Astronautics*, 2017, 38(8): 789-796.

悬吊式重力补偿系统中水平随动机构的动力学分析

王婉情[1], 王庆霞[1,3*], 杨 帅[2], 李 娜[2], 黄顺舟[2,3]
1. 东华大学 机械工程学院, 上海 201620
2. 上海航天设备制造总厂有限公司, 上海 200245
3. 上海航天工艺与装备工程技术研究中心, 上海 200245

摘 要: 针对二维可展开机构的地面试验, 设计了一种悬吊式重力补偿系统: 综合考虑转动随动机构与悬吊机构的刚柔耦合特征, 采用拉格朗日方程推导并建立了以模拟展开物与重力补偿装置为整体的多体动力学模型; 为应对水平方向上由被动跟随所引发的显著非铅锤效应而导致的系统内部瞬时冲击力, 在竖直悬吊机构中串联了弹性元件, 并将其与钢丝绳串联; 利用 ADAMS 软件开展了串联弹性元件对转动随动机构动态响应的分析。仿真分析结果表明, 与无弹性环节相比, 有弹性环节的补偿误差从 45%降低至 0.31%。采用低刚度弹性环节的卸载率要高于采用高刚度弹性环节的卸载率, 在卸载率满足要求的情况下, 选择刚度系数为 6 N/mm 的弹簧进行试验, 得出补偿误差满足设计要求 (5%) 的结论。

关键词: 悬吊式重力补偿; 被动式随动机构; 刚柔耦合模型; 串联弹性元件